Low Resistance Metal Contacts to MoS_2 Devices with Nickel-Etched-Graphene Electrodes

Wei Sun Leong,[||,†] Xin Luo,[||,‡,§] Yida Li,[||,†] Khoong Hong Khoo,[‡,§] Su Ying Quek,[*,‡] and John T. L. Thong[*,†]

[†]Department of Electrical and Computer Engineering, National University of Singapore, Singapore 117583, [‡]Department of Physics, Centre for Advanced 2D Materials and Graphene Research Centre, National University of Singapore, Singapore 117546, and [§]Institute of High Performance Computing, 1 Fusionopolis Way, #16-16 Connexis, Singapore 138632. [||]W.S.L., X.L., and Y.L. contributed equally.

ABSTRACT We report an approach to achieve low-resistance contacts to MoS_2 transistors with the intrinsic performance of the MoS_2 channel preserved. Through a dry transfer technique and a metal-catalyzed graphene treatment process, nickel-etched-graphene electrodes were fabricated on MoS_2 that yield contact resistance as low as 200 $\Omega \cdot \mu$m. The substantial contact enhancement ($\sim$2 orders of magnitude), as compared to pure nickel electrodes, is attributed to the much smaller work function of nickel-graphene electrodes, together with the fact that presence of zigzag edges in the treated graphene surface enhances tunneling between nickel and graphene. To this end, the successful fabrication of a clean graphene–MoS_2 interface and a low resistance nickel–graphene interface is critical for the experimentally measured low contact resistance. The potential of using graphene as an electrode interlayer demonstrated in this work paves the way toward achieving high performance next-generation transistors.

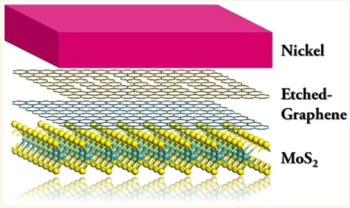

KEYWORDS: Transition metal dichalcogenide · molybdenum disulfide · contact resistance · graphene · field-effect transistor · heterostructure

Two-dimensional transition metal dichalcogenides (TMDs) are materials that present unique electronic and optical properties. Among them, molybdenum disulfide (MoS_2) has received the most attention in recent years. Theoretically, MoS_2 field-effect transistors (FETs) have been predicted to possess reasonable electron mobility, large transconductance, and superior on/off ratios (>10^{10}) due to the large direct band gap (1.9 eV) for monolayer MoS_2.[1−3] More importantly, due to its natural two-dimensional form, MoS_2 is expected to be insusceptible to short channel effects endowing it with great promise as an alternate channel material for postsilicon electronics.[1,3] Despite such potential advantages, in reality, MoS_2 devices with such excellent performance have yet to be realized, with one of the most serious impediments being the nontrivial contact resistance at the metal–MoS_2 interfaces. The large source/drain contact resistance that has been hampering the realization of ideal MoS_2 FETs can be attributed to Fermi level pinning in MoS_2 close to the conduction band edge as a result of sulfur-vacancy defect level and charge neutral level location.[3,4] Regardless of this underlying principle, prior attempts to mitigate this by choosing the most appropriate material as contact metallization to MoS_2 have met with limited success; the lowest contact resistance reported to date using scandium contacts is still far from satisfactory.[3] Alternatively, gas[5] and charge transfer based molecular doping[6] on MoS_2 flakes have been used to lower the contact resistance of MoS_2 devices but accompanying severe degradation in the on/off performance was observed. Recently, chloride molecular doping technique and formation of contacts to metallic-phase MoS_2 have been demonstrated to lower the contact resistance of MoS_2 transistors to 500 $\Omega \cdot \mu$m[7] and 200–300 $\Omega \cdot \mu$m,[8] respectively. Both techniques involve hours of chemical immersion, and how the chemicals affect the MoS_2–dielectric interface requires careful investigation for future technology development.

On the other hand, some research groups have attempted the use of graphene as electrical contacts to MoS_2 devices since it has the ability to enhance electron injection into the conduction band of MoS_2 through lowering of the Schottky barrier height.[9−11]

* Address correspondence to elettl@nus.edu.sg (experiment), phyqsy@nus.edu.sg (theory).

Received for review November 18, 2014 and accepted December 17, 2014.

Published online December 17, 2014
10.1021/nn506567r

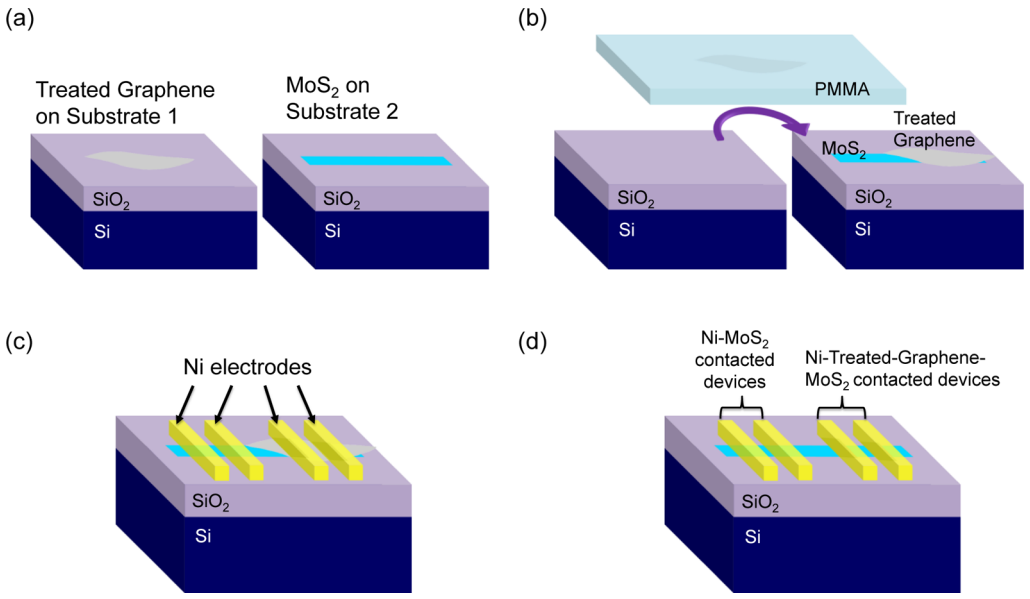

Figure 1. Schematics of the process showing the fabrication steps of a back-gated MoS_2 field-effect transistor with Ni-etched graphene sandwiched at metal−MoS_2 contacts. (a) Exfoliated graphene on a p^+ Si/SiO_2 substrate was first treated with Ni-mediated etching process to create large amount of zigzag edges[13] on the graphene surface while pristine MoS_2 strip was exfoliated on another p^+ Si/SiO_2 substrate. (b) Treated graphene was peeled off from the substrate using Scotch tape technique and transferred onto another substrate with a freshly exfoliated MoS_2 strip on it. For comparison purposes, the treated graphene was aligned to cover half of the MoS_2 strip. (c) Ni metallization deposited as electrical contacts to the MoS_2 device forming both Ni−MoS_2 and Ni-treated graphene−MoS_2 contacts. (d) Exposed graphene was removed completely by utilizing the Ni electrodes as a self-aligned hard mask in combination with a benign oxygen plasma process.

However, graphene by itself as electrode is too thin for electrical characterization (probing) and thus necessitates the use of metal−graphene hybrid as electrical contact for MoS_2 devices.[9,12] The situation at the metal−graphene−MoS_2 contact has become more complicated as it combines both metal−graphene and graphene−MoS_2 interfaces. Taken individually, the former contact resistance is known to be large (up to hundreds of Ω·mm) without any contact treatment, while cleanliness is a key requirement for the latter interface. Failure to optimize either one of these interfaces could compromise the contact enhancement brought about by the graphene interlayer. For example, the contact resistance for Ti-graphene-contacted MoS_2 devices (3.7 ± 0.3 Ω·mm when back gate bias = 30 V)[11] has been reported to be large compared to the lowest contact resistance values reported for MoS_2 devices.[8]

Here, we demonstrate that the resistance of metal contacts to semiconducting-phase MoS_2 can be as low as that of metallic-phase MoS_2 with the use of etched graphene as buffer layer at the metal−MoS_2 interface. To ensure clean graphene−MoS_2 interfaces, a polymer-assisted dry transfer technique is used to layer the graphene onto the MoS_2. Hence, the bottom side of the exfoliated graphene flake, which has never been exposed to any polymer or solvent, is clean and bonds to the MoS_2 crystal lattice through van der Waals force. This is followed by metallization to the graphene using nickel. In order to optimize the metal−graphene interface, we propose to treat the graphene with a nickel-catalyzed etching process prior to stacking on MoS_2, which creates in the graphene a vast density of nanosized pits with zigzag-terminated edges that covalently bond to the deposited nickel (Ni) metallization, thus minimizing the resistance at metal−graphene interface.[13] In brief, the MoS_2 devices with Ni-etched-graphene electrodes show not only about 2 orders of magnitude improvement in contact resistance and 3-fold enhancement in effective mobility, but also performance enhancement in terms of on/off current ratio and subthreshold swing.

RESULTS AND DISCUSSION

The fabrication process of a back-gated MoS_2 FET with Ni-etched graphene sandwiched at metal−MoS_2 contacts is illustrated in Figure 1. In order to carry out a fair comparison between MoS_2 FETs with and without treated graphene as an interlayer at the source/drain contacts, we fabricated on the same MoS_2 strip exfoliated from molybdenite crystal (SPI supplies) an array of MoS_2 back-gated field-effect transistors consisting of both Ni−MoS_2 and Ni-treated graphene−MoS_2 contacts (see Methods for details). Graphene flakes and MoS_2 flakes were first exfoliated onto separate oxidized degenerately p-doped silicon substrate with 285 nm thick SiO_2 (Figure 1a). Exfoliated bilayer graphene (BLG) was identified and then treated with a Ni-catalyzed etching technique,[13] which involves nickel deposition, annealing in hydrogen, and removal of nickel particles by acid. From the other substrate, a freshly exfoliated MoS_2 strip (16 nm thick) with uniform

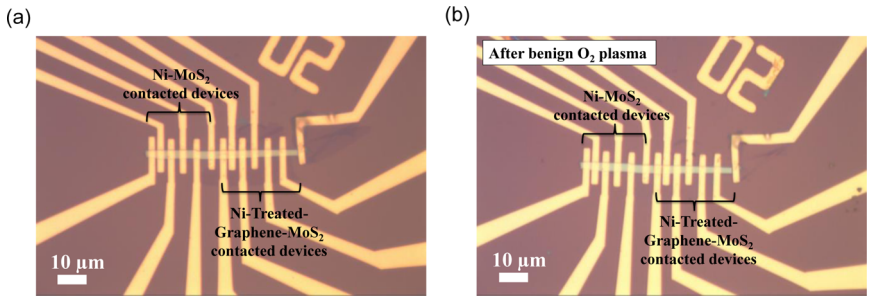

Figure 2. Optical images showing a MoS_2 field-effect transistors array consisting of five Ni-contacted devices and six Ni-treated-graphene-contacted devices with channel lengths varying from 0.5 to 3 μm, in steps of 0.5 μm before (a) and after (b) removal of the exposed graphene by benign oxygen plasma.

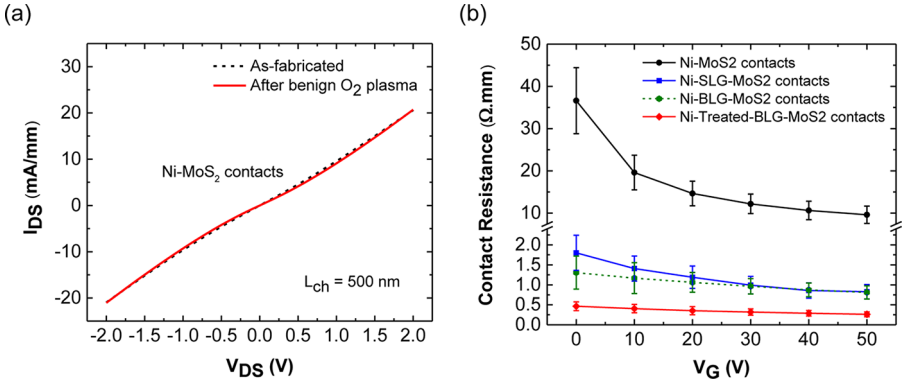

Figure 3. (a) I_D-V_D characteristics of a typical Ni-contacted MoS_2 device shows negligible changes before and after the benign oxygen plasma process. (b) Contact resistance comparison for MoS_2 devices fabricated with four different types of contacts: Ni−MoS_2, Ni−single-layer-graphene−MoS_2, Ni−bilayer-graphene−MoS_2, and Ni-treated-bilayer-graphene−MoS_2 contacts. The lowest R_C of our Ni-treated-bilayer-graphene-contacted MoS_2 devices is as low as 200 $\Omega\cdot\mu$m, which shows ~40 times improvement compared to the Ni-contacted MoS_2 devices.

width (~2 μm) was chosen. Using a polymer-assisted dry transfer technique, the treated graphene was delaminated from its substrate and transferred onto the selected MoS_2 strip (Figure 1b). Thereafter, the source/drain contacts were delineated and metallized with 60 nm of Ni (Figure 1c). Finally, the exposed graphene was completely removed by using the Ni electrodes as a self-aligned hard mask in combination with a benign oxygen plasma process (Figure 1d). As can be seen from Figure 2, the exposed graphene was removed by the oxygen plasma process leaving behind only the MoS_2 as the effective channel for Ni-treated-graphene contacted MoS_2 devices. In addition, the unprotected MoS_2 portion shows no visible damage under an optical microscope. Indeed, the output characteristics of Ni-contacted MoS_2 devices remain unchanged (Figure 3a) prior to and following the benign oxygen plasma process.

For this study, we extracted the contact resistance using transfer length method (TLM). An array of two-terminal devices with Ni−MoS_2 contacts and a corresponding adjacent array of two-terminal devices with Ni-treated-BLG−MoS_2 contacts were fabricated on the same MoS_2 flake of 2 μm width and channel lengths varying from 0.5 to 3 μm, in steps of 0.5 μm (Figure 2b). The two-terminal resistance of each device was measured as a function of back-gate voltage, V_G. Subsequently, the data was fitted using eq 1:

$$R = 2R_C(W) + R_S\frac{L}{W} \quad (1)$$

where R is the two-terminal resistance of each device being measured, R_C is the contact resistance of each contact as a function of width, R_S is the sheet resistance, and L and W represent channel length and width, respectively. Electrical characterizations on all devices were performed in vacuum at room temperature and no annealing was performed prior to measurement.

The extracted R_C as a function of back-gate voltage is plotted in Figure 3b, with error bars that represent uncertainty in the fitting. The R_C of all devices in this study exhibits clear gate-voltage dependence (Figure 3b). This trend corroborates other findings reported in literature,[6,14] where the MoS_2 is electrically doped under high gate bias, resulting in smaller effective Schottky barrier height, and hence the R_C reduces with back-gate bias. As can be seen in Figure 3b, the fitted R_C for devices with Ni-treated-BLG−MoS_2 contacts was found to be 0.26 ± 0.06 and 0.46 ± 0.11 $\Omega\cdot$mm at back-gate biases of 50 and 0 V, respectively, which is within 15% of the MoS_2 FETs' on-resistance and approaches the R_C required for current

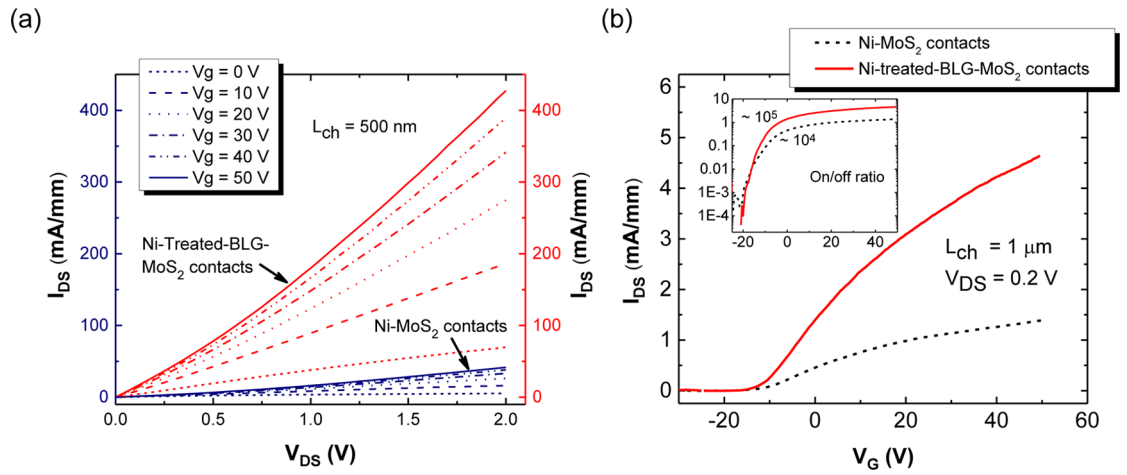

Figure 4. (a) I_D–V_D characteristics of both MoS_2 devices with and without the treated graphene as a sandwich layer. The on-current at V_{DS} = 2 V and V_G = 50 V shows ~10 times improvement, as a result of reduced contact resistance. (b) I_D–V_G characteristics of both MoS_2 devices with and without the treated graphene as a sandwich layer. Inset: I_D–V_G characteristics of the same MoS_2 devices in logarithmic scale. Extrinsic mobility of the typical Ni-treated-bilayer-graphene-contacted MoS_2 device is 3 times higher than that of the Ni-contacted MoS_2 device.

state-of-the-art silicon MOSFETs.[15] On the other hand, the fitted R_C for Ni-contacted MoS_2 devices without any contact interlayer is 9.6 ± 2.1 and 36.6 ± 7.8 Ω·mm at back-gate biases of 50 and 0 V, respectively, which is about 37 and 80 times higher than the fitted R_C of devices with Ni-treated-BLG–MoS_2 contacts, respectively. It should be noted that these two sets of devices were fabricated on the same MoS_2 strip. For comparison purposes, devices with Ni-single-layer-graphene-(SLG)–MoS_2 contacts were fabricated on another MoS_2 strip of a similar thickness and the fitted R_C is also plotted in Figure 3b. The R_C of devices with Ni–SLG–MoS_2 contacts is 0.83 ± 0.18 and 1.80 ± 0.44 Ω·mm at back-gate biases of 50 and 0 V, respectively, which represents 12 and 20 times improvement, respectively, compared to that of pure Ni contacts to MoS_2. On the other hand, with untreated BLG as the contact interlayer, the extracted R_C of 0.81 ± 0.16 and 1.31 ± 0.41 Ω·mm at back-gate biases of 50 and 0 V, respectively, is comparable to that of Ni-SLG-MoS_2 contacts (Figure 3b). Nonetheless, these values are at least 3 times larger than those of Ni-treated-BLG–MoS_2 contacts regardless of back-gate biases. This additional contact enhancement with the use of treated BLG as the contact interlayer, compared to both untreated SLG and BLG, can be attributed to the much smaller resistance at the Ni-graphene interface as illustrated by Figure S1 in the Supporting Information. In spite of that, the use of treated SLG as the contact interlayer showed inferior contact performance compared to that of untreated SLG (Table S1). This can be attributed to the perforated treated SLG contact interlayer that no longer prevents direct interaction between Ni and MoS_2 atoms.

It should be noted that the Ni-catalyzed etching treatment performed on graphene (either SLG or BLG) is capable of creating a significant amount of zigzag graphene edges (either triangular or hexagonal nano-sized pits)[13] in the graphene surface (see Supporting Information S3 for details). More importantly, these zigzag graphene edges are expected to directly bond to the subsequent nickel metallization in end-contacted geometry,[13] rather than the surface-contacted geometry, and thus results in metal–graphene interfaces with smaller contact resistance ($R_{edge} \ll R_{surface}$) as has been predicted theoretically[16] and proven experimentally.[17,18] In addition, due to weak van der Waals bonds, the tunneling resistance between graphene layers in BLG is found to be larger compared to that of end-contacted metal–graphene contacts ($R_{edge} \ll R_{interlayer}$)[19] and hence graphite (>2 layers of graphene) should be avoided to minimize the contribution of tunneling resistance between graphene layers. In brief, the results show that insertion of graphene as an interlayer by itself already enhances the carrier injection at the metal–MoS_2 contacts, and the use of the Ni-catalyzed etching technique further boosts the carrier injection at the metal–MoS_2 contacts.

In Figure 4, we compare the output and transfer characteristics of two MoS_2 FETs with different types of contacts: Ni–MoS_2 and Ni-treated-BLG–MoS_2 contacts. Both FETs were fabricated with the same device dimensions and on the same MoS_2 flake. Electrical characterization were performed in vacuum at room temperature. As can be seen from Figure 4a, the MoS_2 devices show ~10 times improvement in terms of on-current at V_{DS} = 2 V and V_G = 50 V with the insertion of treated graphene as a sandwich layer at metal–MoS_2 contacts. This observation is consistent across all the fabricated FETs regardless of the channel length. In addition, back-gate measurements were also performed on these pairs of MoS_2 FETs and both FETs exhibit n-type behavior with similar threshold voltage.

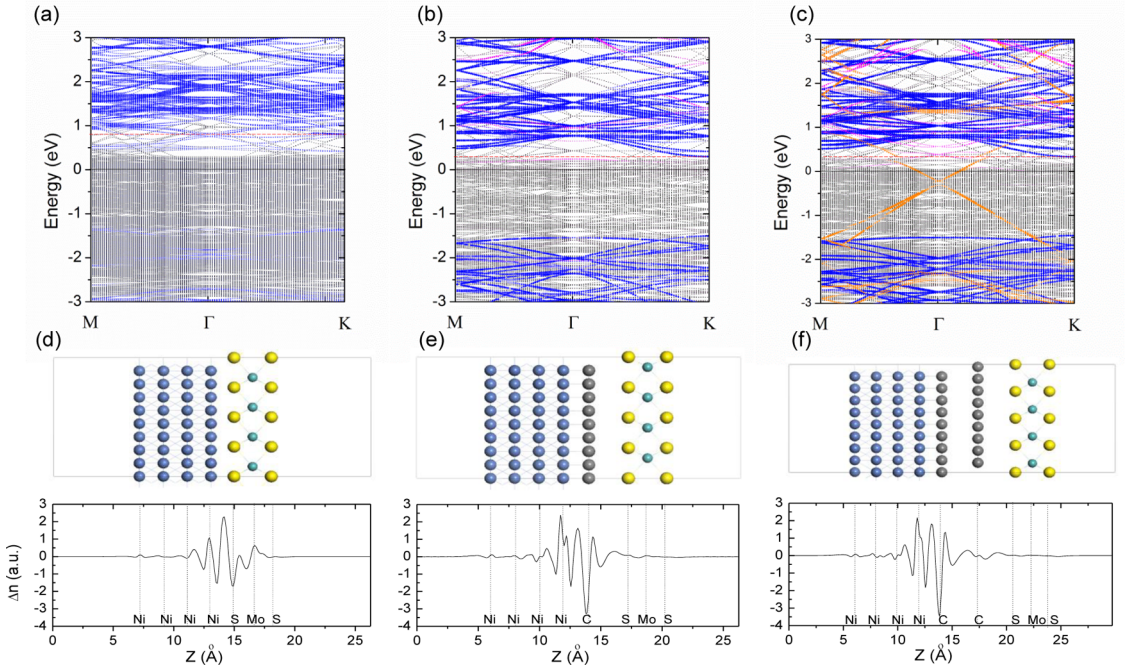

Figure 5. Band structures of single layer MoS_2 interfaced with (a) Ni, (b) Ni-SLG, and (c) Ni-BLG, only the minority bands are shown here for magnetic systems. Blue, pink, and orange dots represent the projected bands of MoS_2, graphene layer close to Ni, and graphene layer adjacent to MoS_2, respectively, with the projection weight indicated by the dot size. Black solid curves and red dashed curves show the positions of the Fermi level and conduction band minimum of MoS_2, respectively. The side views of the atomic structures and plane averaged charge differences Δn along the z direction are shown below the band structures in panels (d)−(f). Δn is obtained by subtracting the plane-averaged charge density of the composite slab from that of individual components of the slab using the same supercell, that is, $\Delta n = n_{Ni-graphene-MoS_2}(z) - n_{Ni}(z) - n_{graphene}(z) - n_{MoS_2}(z)$.

This implies that the treated-graphene sandwich layer at metal-MoS_2 contacts induces no doping. Moreover, the typical MoS_2 devices with Ni-treated-BLG−MoS_2 contacts exhibit larger on/off current ratio (10^5) and better subthreshold swing (3.7 V/decade at $V_{DS} = 0.2$ V) compared to those of Ni−MoS_2 contacts (10^4 and 6.7 V/decade at $V_{DS} = 0.2$ V) as can be seen from the inset of Figure 4b. We then extract the extrinsic mobility of these pairs of MoS_2 FETs using eq 2:

$$\mu = \frac{1}{C_{ox} V_{DS}} \frac{L_{ch}}{W_{ch}} \frac{\Delta I_{DS}}{\Delta V_G} \qquad (2)$$

where C_{ox} is the gate capacitance (1.21×10^{-8} F/cm^2 for 285 nm thick SiO_2), L_{ch} and W_{ch} are channel length and width, respectively, I_{DS} is the drain current, V_{DS} is the drain voltage, and V_G is the gate voltage. The electron mobility for the typical device with Ni-treated-BLG−MoS_2 contacts is 80 cm^2/V-s, while for the device with Ni−MoS_2 contacts is 27 cm^2/V·s. This 3-fold improvement in extrinsic mobility can be attributed to the reduced contact resistance. It is worth noting that both the contact resistance and mobility values reported here can be better by elimination of residual PMMA left over by the lithography and polymer-assisted dry transfer processes.

We now elucidate, using first-principles calculations, the essential physics behind the observed smaller contact resistance in Ni-treated-BLG−MoS_2 compared to Ni−MoS_2 contacts. Since the largest reduction in contact resistance occurs when Ni−MoS_2 contacts are replaced by Ni−SLG−MoS_2 and Ni−BLG−MoS_2 contacts (Figure 3b), we first focus on the effect of inserting SLG and BLG at the Ni−MoS_2 contacts. The Schottky barrier height (SBH) is a key factor that determines contact resistances in semiconductor MOSFETs, and in particular in the MoS_2 transistors considered here.[20] We therefore perform a comparative SBH analysis on Ni−MoS_2, Ni−SLG−MoS_2, and Ni−BLG−MoS_2 interfaces. Figure 5 shows the calculated minority spin bands and side views of the corresponding optimized atomic structures, while the majority spin bands and top view of the atomic structures are presented in Figure S4. When MoS_2 is in direct contact with Ni, the binding energy between them is large and the equilibrium interface distance is only 1.92 Å, smaller than the value of 2.08 Å for graphene chemisorbed on Ni. The strong binding influences the electronic structure, as can be seen in Figure 5a, where the projected band structure on MoS_2 (represented by blue dots with the projection weight represented by dot size), is strongly perturbed and bears little resemblance to that of pristine MoS_2 (Figure S4). For the Ni−SLG−MoS_2 contact, graphene p_z-states (represented by magenta dots in Figure 5b) hybridize strongly with the Ni d-states, and serve as a buffer layer separating the MoS_2 from Ni. Therefore, the projected band structure of MoS_2 is similar to that of an isolated MoS_2 layer (Figures 5b and S4). In both cases, the Fermi level is closer to the

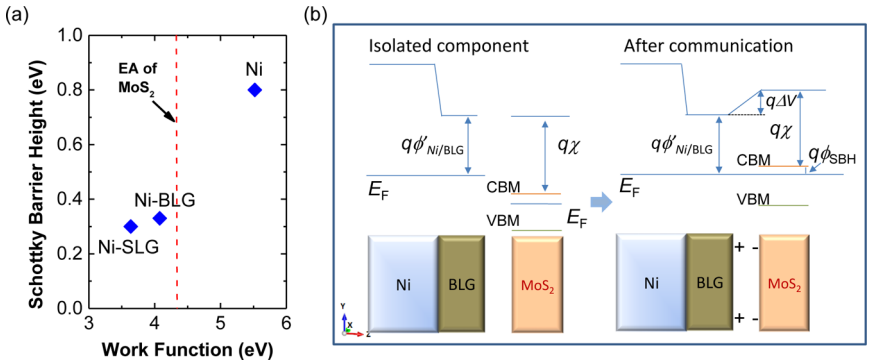

Figure 6. (a) Plot of calculated Schottky barrier height as a function of the electrode work function; the electron affinity (EA) of MoS_2 is shown as the red dashed line. (b) Schematic illustration of the potential shift at the interface of the Ni−BLG−MoS_2 system.

MoS_2 conduction band minimum (CBM) than to the valence band maximum (VBM), so that the SBH is extracted by taking the energy difference between the Fermi level of the electrode and the CBM of MoS_2 (Figure 6). Remarkably, the extracted SBH is reduced from 0.8 to 0.3 eV with the insertion of a graphene layer at the Ni−MoS_2 contacts (Figure 6a). The accuracy of our calculated SBH is verified using higher convergence criteria (Table S2). With the insertion of BLG as a contact interlayer at the Ni−MoS_2 contacts, Ni states are sufficiently isolated from MoS_2 and its adjoining graphene layer (Figure 5). Thus, we can see an intact MoS_2 projected band structure and a graphene projected band structure that exhibits clear graphene characteristics (represented by orange dots in Figure 5c), such as the Dirac conical points which are shifted from the K-point to the Γ-point due to Brillouin zone folding. The extracted SBH for Ni−BLG−MoS_2 contacts is very similar to that for Ni−SLG−MoS_2 contacts (Figure 6a).

Generally, it has been found that the SBH at metal−MoS_2 contacts increases as the work function of the contacting metal electrode increases.[20−22] This trend makes sense considering the fact that the SBH at metal−MoS_2 contacts is computed as the difference between the Fermi level of the electrode and the CBM of MoS_2; in experiments, the SBH is more accurately given by the difference between the Fermi level of the electrode and the defect levels in MoS_2 (which are also close to the CBM).[2,23] In the simplest consideration, in order for the Fermi level not to fall too far into the band gap of MoS_2, the ideal electrode would be one whose work function is as close as possible to (or if not, smaller than) the electron affinity of MoS_2. In Figure 6a, the SBHs from our calculations are plotted against the work functions of different electrodes (i.e., Ni, Ni−SLG, and Ni−BLG). These plots strongly suggest that the significant reduction of the SBH is closely related to the reduction of the work function of the Ni−graphene electrodes (both Ni−SLG and Ni−BLG electrodes) compared to that of Ni electrodes. The calculated work functions, $q\phi_M$ of the Ni-graphene electrodes (3.64 eV for Ni−SLG and 4.08 eV for Ni−BLG) are smaller than the calculated electron affinity, $q\chi$, of isolated MoS_2 (4.33 eV); in contrast, the work function of Ni is significantly higher (5.52 eV). As the work function of Ni is substantially larger than the electron affinity of MoS_2, even with partial Fermi level pinning from metal-induced gap states at the strongly hybridized Ni−MoS_2 interface,[21] the resulting SBH is still quite large. On the other hand, due to the weak van der Waals interactions between graphene and MoS_2, Ni−graphene electrodes interact with MoS_2 mainly by charge transfer, which determines the resulting SBH. Specifically, one expects electrons to be transferred from the electrodes to MoS_2, resulting in an interface dipole that raises the relative potential at MoS_2, giving rise to a small SBH (Figure 6b). By comparing the magnitude of the dipole at the electrode−MoS_2 interface, we found that the dipole moment is stronger in the Ni−SLG−MoS_2 interfaces compared to that of Ni−BLG−MoS_2, causing a larger upward shift of the MoS_2 bands. This is why even though the work function of the Ni−SLG electrode is 0.4 eV smaller than that of the Ni−BLG electrode, the SBH is comparable in both Ni−SLG−MoS_2 and Ni−BLG−MoS_2 interfaces. Figure 5d−f shows the plane-averaged charge difference Δn obtained by subtracting the plane-averaged charge density of the composite slab from that of individual components of the slab using the same supercell, that is, $\Delta n = n_{Ni-graphene-MoS_2}(z) - n_{Ni}(z) - n_{graphene}(z) - n_{MoS_2}(z)$. These plots give further evidence that the interaction between MoS_2 and the electrode is larger for the bare Ni electrodes than for the Ni−graphene electrodes. On the other hand, the complicated charge density profile at the Ni−graphene interface shows that there is strong interaction between Ni and graphene, which explains the large reduction in work function of the Ni-graphene electrodes.[24]

The above discussion indicates that the large reduction in contact resistance going from Ni−MoS_2 interfaces to Ni−SLG−MoS_2 and Ni−BLG−MoS_2 interfaces arises from the reduction in SBH due to the significantly smaller work functions of the Ni−graphene electrodes (both Ni−SLG and Ni−BLG electrodes). As we have seen in the literature,[20,21] the computed SBH is

expected to be slightly larger than the experimentally extracted SBH, partly due to the neglect of defect levels and to the fact that monolayer MoS_2 is considered in the calculations. However, the trends predicted by theory have been shown to be robust[20,21] and we expect that the large change in SBH predicted here also exists in experiment.

Moving on to explain the further reduction in contact resistance going from Ni-BLG-MoS_2 to Ni-treated-BLG−MoS_2 interfaces, we consider the effects of zigzag graphene edges at the Ni−graphene interface (Figure S5a-b). It is interesting that our computed SBH for Ni-treated-BLG−MoS_2 interfaces is very similar to that of Ni−BLG−MoS_2 interfaces. Furthermore, by performing nonequilibrium Green's function (NEGF) density functional theory calculations,[25] we find that the contact resistance of zigzag-edge-contacted Ni−graphene interface (233 $\Omega\cdot\mu$m) is significantly smaller than that of surface-contacted Ni−graphene interface (340 $\Omega\cdot\mu$m; see Methods for details and Figure S6 for geometries). Similar calculations comparing surface and edge-contacted graphene by other metals have also found edge-contacted metal−graphene interfaces to yield lower contact resistances, due to the stronger metal−graphene coupling at these interfaces.[16] Therefore, we can infer that the effect of Ni-mediated etching treatment on reducing the contact resistance arises primarily from the stronger coupling between Ni and zigzag graphene edges. It is important to note that although stronger coupling can reduce the contact resistance as shown here, tunnelling probabilities depend exponentially on the SBH; therefore, the reduction in SBH going from Ni−MoS_2 to Ni−graphene−MoS_2 interfaces has a larger effect on the contact resistance than the extent of coupling between MoS_2 and the electrodes, which we have not considered here. We also find that the SBH of Ni-treated-SLG−MoS_2 interfaces is slightly larger than those of Ni−SLG−MoS_2 and Ni−BLG−MoS_2 interfaces, but smaller than that of Ni−MoS_2 interfaces (Table S2, Figure S5c). These results are consistent with the contact resistances measured in experiment (Table S1).

CONCLUSIONS

We have shown that the insertion of graphene as a contact interlayer into Ni−MoS_2 contacts can significantly reduce the contact resistance. A further treatment of the bilayer graphene surface, namely, Ni-mediated etching, can further reduce the contact resistance. Sets of TLM structures consisting of multiple FETs each were fabricated with four types of contact structures: Ni−MoS_2, Ni−SLG−MoS_2, Ni−BLG−MoS_2, and Ni-treated-BLG−MoS_2 contacts on exfoliated MoS_2 of similar thickness. Electrical measurements made on all sets of FETs indicate that the contact resistance of the Ni−SLG−MoS_2 FETs is significantly reduced by 20-fold as compared to the Ni−MoS_2 FETs, and is further reduced by an additional 3-fold for the FETs with Ni-treated-BLG−MoS_2 contacts. This significant contact enhancement results in improved field-effect mobility in the FETs with treated-BLG as a contact interlayer, compared to the more traditional FETs with pure Ni as the contact electrodes (80 versus 27 $cm^2/V\cdot s$). From our $I-V$ measurements, it is clear that regardless of the insertion of untreated or treated graphene at the contacts, a much lower effective Schottky barrier height can be observed. First-principles calculations indicate that the large reduction in contact resistance observed experimentally results from the lower work function in the Ni−graphene electrodes, resulting in a smaller SBH in Ni−graphene−MoS_2 contacts. The effect of Ni-mediated etching treatment of bilayer graphene further reduces the contact resistance due to stronger coupling between Ni and the zigzag graphene edges. The significant contact resistance reduction, and enhancement of the on/off ratio, subthreshold-swing and mobility with the use of graphene as the contact interlayer is remarkable considering the fact that there is no systematic method reported to date to improve the contact and adhesion of metal to MoS_2. Our findings provide an insight into how the contact resistance at metal-MoS_2 contacts can be engineered with the use of graphene as an interlayer. Moreover, the proposed Ni-mediated etching treatment for graphene that further lowers the contact resistance is compatible with semiconductor industry manufacturing technology. Hence, with the approach demonstrated in this work, the use of MoS_2 as a mainstream electronic material is brought one step closer to the forefront.

METHODS

Fabrication of MoS_2 Field-Effect Transistor with Ni-Etched Graphene Sandwiched at Metal−MoS_2 Contacts. MoS_2 and graphene flakes were first exfoliated on separate oxidized degenerately p-doped silicon substrate with 285 nm thick SiO_2 (Figure 1a). The exfoliated bilayer graphene was then treated with a Ni-catalyzed etching technique.[13] This started with the deposition of a thin film (2 nm) of Ni on the exfoliated graphene via thermal evaporation at a rate of 0.1 nm per second. Subsequently, the graphene sample was annealed at 580 °C for 10 min in a hydrogen ambient and a significant amount of etched pits with well-defined zigzag edges is created on the graphene basal plane based on a Ni-catalyzed gasification process: C (solid) + $2H_2$ (gas) → CH_4 (gas).[13] Thereafter, all nickel particles were removed using acid. This was followed by spin-coating of a poly(methyl methacrylate) (PMMA) layer (600 nm thick) and baked at 120 °C in an oven for 10 min. The PMMA film with the graphene was then delaminated from the substrate using a Scotch tape and transferred onto the targeted substrate with the freshly exfoliated MoS_2 strip (16 nm thick) of uniform width (~2 μm) (Figure 1b). For this dry transfer technique, a micromanipulator was used to align the treated-graphene to the

exfoliated MoS_2 (Figure 1c). The sample was then baked at 100 °C to improve adhesion. Subsequently, the source/drain contacts were delineated and metallized with 60 nm of Ni (Figure 1c). Finally, the exposed graphene was completely removed by utilizing the Ni electrodes as a self-aligned hard mask in combination with a benign oxygen plasma process (10 W RF power, 30 V substrate bias, for 30 s). Electrical characterization on all devices were performed at room temperature in a high vacuum chamber (10^{-6} mbar) to avoid unnecessary interaction with moisture in ambient.[26]

First-Principles Calculations. The first-principles calculations are performed using a plane wave basis set at the level of density functional theory (DFT), as implemented in the VASP code.[27] The local spin density approximation (LSDA)[28] is employed for the exchange-correlation functional and projector-augmented wave (PAW)[29] potentials are used throughout the calculation. The (111) surface of Ni has similar lattice constants with graphene. To construct a commensurate interface between Ni-graphene/Ni and MoS_2, we use a rotated 30° 6×6 supercell of graphene to accommodate the MoS_2 4×4 supercell, and the Ni electrode is modeled by a slab consisting of four atomic layers of Ni. The constructed structures have about 1% compressive strain in graphene and such supercells have been observed experimentally.[30] A plane wave kinetic energy cutoff of 450 eV is used for the wave function basis set, and a gamma centered $3 \times 3 \times 1$ k-point grid is sampled in the Brillouin zone (BZ). Increasing the cutoff energy and k-point grid only leads to minor differences with the present results (Table S2). Dipole corrections are applied in the self-consistent calculations to prevent interactions between moments of different supercells. The slabs are separated by a vacuum of at least 12 Å to prevent interactions between periodic image slabs. The interface structures and internal coordinates are fully relaxed with fixed lattice constants such that the maximum component of the Hellmann−Feynman force acting on each ion is less than 0.02 eV/Å. In the work function calculations, the unit cells of Ni, Ni−SLG, and Ni−BLG are used together with a much denser BZ k-point sampling of $44 \times 44 \times 1$. The energy convergence threshold is set at 10^{-6} eV.

It is worth noting that the computed work functions in this work are consistent with the values in prior experimental works. The calculated work function of our Ni and Ni-SLG electrodes are respectively 5.52 and 3.64 eV, consistent with previous DFT calculations,[31] and also close to the experimental values (5.35 eV for Ni and 3.9 eV for Ni−SLG).[32,33]

NEGF-DFT calculations were performed using the ATOMISTIX TOOLKIT (ATK) package, that employs a numerical localized basis sets and the nonequilibrium Green's function (NEGF) formalism. Self-consistent calculations were performed using a double-ξ polarized basis set and a density mesh cutoff of 300 Ry. Exchange correlation was treated using the local spin density approximation[28] and all atoms were relaxed such that the force per atom was less than 0.05 eV/Å. The k-point samplings of 15×1 and 15×4 were employed for the surface- and edge-contacted interfaces respectively along the in-plane directions. To obtain the transmission spectrum, a denser k-point grid of 500×1 and 500×50 was used for the side and edge contact interfaces respectively along the in-plane directions. Figure S6 shows the geometries. The contact resistance was obtained from the calculated transmission spectra $T(E)$ using the formula

$$R_C = \left(\int T(E) \frac{e^{(E - E_F)/k_B T}}{(e^{(E - E_F)/k_B T} + 1)^2} \frac{dE}{k_B T} \right)^{-1}$$

with the temperature set to 300 K.

Conflict of Interest: The authors declare no competing financial interest.

Acknowledgment. This project is supported by Grant R-263-000-A76-750 from the Faculty of Engineering, NUS and Grant NRF-NRFF2013-07 from the National Research Foundation, Singapore.

Supporting Information Available: Average contact resistance on MoS_2 devices fabricated using different electrodes, comparison of the resistor network models at the metal−MoS_2 contacts with bilayer graphene and treated bilayer graphene as a sandwich layer, characterization of bilayer graphene after the Ni-catalyzed etching treatment, band structure of MoS_2 interfaced with different electrodes, NEGF-DFT calculations of surface-contacted and edge-contacted Ni-graphene interface, Figures S1−S6 and Tables S1, S2. This material is available free of charge *via* the Internet at http://pubs.acs.org.

REFERENCES AND NOTES

1. Yoon, Y.; Ganapathi, K.; Salahuddin, S. How Good Can Monolayer MoS_2 Transistors Be? *Nano Lett.* **2011**, *11*, 3768–3773.
2. Radisavljevic, B.; Radenovic, A.; Brivio, J.; Giacometti, V.; Kis, A. Single-Layer MoS_2 Transistors. *Nat. Nanotechnol.* **2011**, *6*, 147–150.
3. Das, S.; Chen, H.-Y.; Penumatcha, A. V.; Appenzeller, J. High Performance Multilayer MoS_2 Transistors with Scandium Contacts. *Nano Lett.* **2013**, *13*, 100–105.
4. Liu, D.; Guo, Y.; Fang, L.; Robertson, J. Sulfur Vacancies in Monolayer MoS_2 and Its Electrical Contacts. *Appl. Phys. Lett.* **2013**, *103*, 183113−1–183113−4.
5. Fang, H.; Tosun, M.; Seol, G.; Chang, T. C.; Takei, K.; Guo, J.; Javey, A. Degenerate n-Doping of Few-Layer Transition Metal Dichalcogenides by Potassium. *Nano Lett.* **2013**, *13*, 1991–1995.
6. Du, Y.; Liu, H.; Neal, A. T.; Mengwei, S.; Ye, P. D. Molecular Doping of Multilayer MoS_2 Field-Effect Transistors: Reduction in Sheet and Contact Resistances. *IEEE Electron Device Lett.* **2013**, *34*, 1328–1330.
7. Yang, L.; Majumdar, K.; Liu, H.; Du, Y.; Wu, H.; Hatzistergos, M.; Hung, P. Y.; Tieckelmann, R.; Tsai, W.; Hobbs, C.; Ye, P. D. Chloride Molecular Doping Technique on 2D Materials: WS2 and MoS_2. *Nano Lett.* **2014**, *14*, 6275–6280.
8. Kappera, R.; Voiry, D.; Yalcin, S. E.; Branch, B.; Gupta, G.; Mohite, A. D.; Chhowalla, M. Phase-Engineered Low-Resistance Contacts for Ultrathin MoS_2 Transistors. *Nat. Mater.* **2014**, *13*, 1128–1134.
9. Roy, T.; Tosun, M.; Kang, J. S.; Sachid, A. B.; Desai, S.; Hettick, M.; Hu, C. C.; Javey, A. Field-Effect Transistors Built from All Two-Dimensional Material Components. *ACS Nano* **2014**, *8*, 6259–6264.
10. Yoon, J.; Park, W.; Bae, G.-Y.; Kim, Y.; Jang, H. S.; Hyun, Y.; Lim, S. K.; Kahng, Y. H.; Hong, W.-K.; Lee, B. H.; et al. Highly Flexible and Transparent Multilayer MoS_2 Transistors with Graphene Electrodes. *Small* **2013**, *9*, 3295–3300.
11. Du, Y.; Yang, L.; Zhang, J.; Liu, H.; Majumdar, K.; Kirsch, P. D.; Ye, P. D. MoS_2 Field-Effect Transistors With Graphene/Metal Heterocontacts. *IEEE Electron Device Lett.* **2014**, *35*, 599–601.
12. Yu, L.; Lee, Y.-H.; Ling, X.; Santos, E. J. G.; Shin, Y. C.; Lin, Y.; Dubey, M.; Kaxiras, E.; Kong, J.; Wang, H.; et al. Graphene/MoS_2 Hybrid Technology for Large-Scale Two-Dimensional Electronics. *Nano Lett.* **2014**, *14*, 3055–3063.
13. Leong, W. S.; Gong, H.; Thong, J. T. L. Low-Contact-Resistance Graphene Devices with Nickel-Etched-Graphene Contacts. *ACS Nano* **2014**, *8*, 994–1001.
14. Liu, H.; Neal, A. T.; Ye, P. D. Channel Length Scaling of MoS_2MOSFETs. *ACS Nano* **2012**, *6*, 8563–8569.
15. Liu, R. *Process Integration, Devices, and Structures*; International Technology Roadmap for Semiconductors, 2012; http://www.itrs.net/Links/2012ITRS/Home2012.htm.
16. Matsuda, Y.; Deng, W.-Q.; Goddard, W. A. Contact Resistance for "End-Contacted" Metal−Graphene and Metal−Nanotube Interfaces from Quantum Mechanics. *J. Phys. Chem. C* **2010**, *114*, 17845–17850.
17. Wang, L.; Meric, I.; Huang, P. Y.; Gao, Q.; Gao, Y.; Tran, H.; Taniguchi, T.; Watanabe, K.; Campos, L. M.; Muller, D. A.; et al. One-Dimensional Electrical Contact to a Two-Dimensional Material. *Science* **2013**, *342*, 614–617.
18. Leong, W. S.; Nai, C. T.; Thong, J. T. L. What Does Annealing Do to Metal−Graphene Contacts? *Nano Lett.* **2014**, *14*, 3840–3847.

19. Chu, T.; Chen, Z. Understanding the Electrical Impact of Edge Contacts in Few-Layer Graphene. *ACS Nano* **2014**, *8*, 3584–3589.
20. Das, S.; Appenzeller, J. Where Does the Current Flow in Two-Dimensional Layered Systems? *Nano Lett.* **2013**, *13*, 3396–3402.
21. Gong, C.; Colombo, L.; Wallace, R. M.; Cho, K. The Unusual Mechanism of Partial Fermi Level Pinning at Metal−MoS_2 Interfaces. *Nano Lett.* **2014**, *14*, 1714–1720.
22. Chen, W.; Santos, E. J. G.; Zhu, W.; Kaxiras, E.; Zhang, Z. Tuning the Electronic and Chemical Properties of Monolayer MoS_2 Adsorbed on Transition Metal Substrates. *Nano Lett.* **2013**, *13*, 509–514.
23. Yu, W. J.; Li, Z.; Zhou, H.; Chen, Y.; Wang, Y.; Huang, Y.; Duan, X. Vertically Stacked Multi-Heterostructures of Layered Materials for Logic Transistors and Complementary Inverters. *Nat. Mater.* **2013**, *12*, 246–252.
24. Giovannetti, G.; Khomyakov, P. A.; Brocks, G.; Karpan, V. M.; van den Brink, J.; Kelly, P. J. Doping Graphene with Metal Contacts. *Phys. Rev. Lett.* **2008**, *101*, 026803.
25. Brandbyge, M.; Mozos, J.-L.; Ordejón, P.; Taylor, J.; Stokbro, K. Density-Functional Method for Nonequilibrium Electron Transport. *Phys. Rev. B* **2002**, *65*, 165401.
26. Qiu, H.; Pan, L.; Yao, Z.; Li, J.; Shi, Y.; Wang, X. Electrical Characterization of Back-Gated Bi-layer MoS_2 Field-Effect Transistors and The Effect of Ambient on Their Performances. *Appl. Phys. Lett.* **2012**, *100*, 123104-1–123104-3.
27. Kresse, G.; Furthmüller, J. Efficient Iterative Schemes for *Ab Initio* Total-Energy Calculations Using a Plane-Wave Basis Set. *Phys. Rev. B* **1996**, *54*, 11169–11186.
28. Perdew, J. P.; Zunger, A. Self-Interaction Correction to Density-Functional Approximations for Many-Electron Systems. *Phys. Rev. B* **1981**, *23*, 5048–5079.
29. Blöchl, P. E. Projector Augmented-Wave Method. *Phys. Rev. B* **1994**, *50*, 17953–17979.
30. Coy Diaz, H.; Addou, R.; Batzill, M. Interface Properties of CVD Grown Graphene Transferred onto MoS_2(0001). *Nanoscale* **2014**, *6*, 1071–1078.
31. Khomyakov, P. A.; Giovannetti, G.; Rusu, P. C.; Brocks, G.; van den Brink, J.; Kelly, P. J. First-Principles Study of The Interaction and Charge Transfer between Graphene and Metals. *Phys. Rev. B* **2009**, *79*, 195425.
32. Michaelson, H. B. The Work Function of the Elements and its Periodicity. *J. Appl. Phys.* **1977**, *48*, 4729–4733.
33. Oshima, C.; Nagashima, A. Ultra-Thin Epitaxial Films of Graphite and Hexagonal Boron Nitride on Solid Surfaces. *J. Phys.: Condens. Matter* **1997**, *9*, 1.